

Simultaneous Estimation of Time Delays and Quasar Structure¹

Christopher W. Morgan² and Michael E. Eyler

*Department of Physics, United States Naval Academy, 572C Holloway Road, Annapolis, MD
21402*

C.S. Kochanek and Nicholas D. Morgan

*Department of Astronomy, The Ohio State University, 140 West 18th Avenue, Columbus, OH
43210 -1173*

Emilio E. Falco

Harvard-Smithsonian Center for Astrophysics, 60 Garden Street, Cambridge, MA, 02138

and

C. Vuissoz, F. Courbin and G. Meylan

*Laboratoire d'Astrophysique, École Polytechnique Fédérale de Lausanne (EPFL), Observatoire,
1290 Sauverny, Switzerland*

ABSTRACT

We expand our Bayesian Monte Carlo method for analyzing the light curves of gravitationally lensed quasars to simultaneously estimate time delays and quasar structure including their mutual uncertainties. We apply the method to HE1104–1805 and QJ0158–4325, two doubly-imaged quasars with microlensing and intrinsic variability on comparable time scales. For HE1104–1805 the resulting time delay of $\Delta t_{AB} = t_A - t_B = 162.2_{-5.9}^{+6.3}$ days and accretion disk size estimate of $\log(r_s/\text{cm}) = 15.7_{-0.5}^{+0.4}$ at $0.2\mu\text{m}$ in the rest frame are consistent with earlier estimates but suggest that existing methods for estimating time delays in the presence of microlensing underestimate the uncertainties. We are unable to measure a time delay for QJ0158–4325, but the accretion disk size is $\log(r_s/\text{cm}) = 14.9 \pm 0.3$ at $0.3\mu\text{m}$ in the rest frame.

Subject headings: cosmology:observations — accretion, accretion disks — dark matter — gravitational lensing — quasars: general

²Department of Astronomy, The Ohio State University

¹Based on observations obtained with the Small and Moderate Aperture Research Telescope System (SMARTS)

1. Introduction

Variability in lensed quasar images comes from two very different sources. Changes in the quasar’s intrinsic luminosity are observable as correlated variability between images, while microlensing by the stars in the lens galaxy produces uncorrelated variability. Measurements of the time delays between the lensed images from the correlated variability can be used to study cosmology (e.g. Refsdal 1964 and recently Saha et al. 2006; Oguri 2007) or the distribution of dark matter in the lens galaxy (e.g. Kochanek et al. 2006; Poindexter et al. 2007; Vuissoz et al. 2007). The microlensing variability can be used to study the structure of the quasar, the masses of the stars in the lens galaxy, and the stellar mass fraction near the lensed images (Schechter & Wambsganss 2002; Wambsganss 2006). It is now possible to use microlensing to measure the correlation of accretion disk size with black hole mass (Morgan et al. 2007), the wavelength dependence of the size of the accretion disk (Poindexter, Morgan & Kochanek 2007) or the differing sizes of the thermal and non-thermal X-ray emission regions (Pooley et al. 2007; Dai et al. 2007).

The challenge is that most lensed quasars exhibit both intrinsic and microlensing variability. To measure a time delay, one must successfully model and remove the microlensing variability such that only intrinsic variability remains. If the microlensing variability has a sufficiently low amplitude or long timescale, it can be ignored (e.g. PG1115-080, Schechter et al. 1997), but this is a dangerous assumption for many systems. Eigenbrod et al. (2005) found that for an 80 day delay, adding microlensing perturbations with an amplitude of 5% (10%) to a light curve increased the uncertainty in the time delay by a factor of 2 (6). Existing time delay analyses for lenses with microlensing (e.g. Paraficz et al. 2006; Kochanek et al. 2006; Poindexter et al. 2007) depend on the intrinsic and microlensing variability having different time scales. These analyses also require that the microlensing variability can be modeled by a simple polynomial function. This approach will clearly fail if the two sources of variability have similar time scales or if the microlensing variability cannot be easily parameterized.

In this paper, we present a new technique for simultaneously estimating the time delay and structure of lensed quasars that exhibit strong microlensing. In essence, we assume a range of time delays and then determine the likelihood of the implied microlensing variability using the Bayesian Monte Carlo method of Kochanek (2004, see also Kochanek et al. 2007). This allows us to estimate the time delays and the quasar structural parameters simultaneously and include the effects of both phenomena on the parameter uncertainties. We apply the method to the two

1.3m, which is operated by the SMARTS Consortium, the Apache Point Observatory 3.5m telescope, which is owned and operated by the Astrophysical Research Consortium, the WIYN Observatory which is owned and operated by the University of Wisconsin, Indiana University, Yale University and the National Optical Astronomy Observatories (NOAO), the 6.5m Magellan Baade telescope, which is a collaboration between the observatories of the Carnegie Institution of Washington (OCIW), University of Arizona, Harvard University, University of Michigan, and Massachusetts Institute of Technology, and observations made with the NASA/ESA Hubble Space Telescope for program HST-GO-9744 of the Space Telescope Science Institute, which is operated by the Association of Universities for Research in Astronomy, Inc., under NASA contract NAS 5-26555.

doubly-imaged lenses HE1104–1805 (Wisotzki et al. 1993) and QJ0158–4325 (Morgan et al. 1999). While HE1104–1805 has a well-measured time delay (Poindexter et al. 2007), the amplitude of the microlensing (~ 0.05 mag yr $^{-1}$ over the past decade) and the fact that it exhibits variability on the 6 month scale of the time delay suggest that it is close to the limit where microlensing polynomial fitting methods (Burud et al. 2001; Kochanek et al. 2006) will break down. QJ0158–4325 clearly shows both correlated and uncorrelated variability, but the polynomial methods cannot reliably produce a time delay estimate. We describe the data and our models in §2, our new approach in §3 and the application to the two systems in §4. In §5, we discuss the results and their limitations. We assume a flat $\Omega_0 = 0.3$, $\Lambda_0 = 0.7$, $H_0 = 70$ km s $^{-1}$ Mpc $^{-1}$ cosmology and that the lens redshift of QJ0158–4325 is $z_l = 0.5$. Reasonable changes in this assumed redshift have negligible consequences for the results.

2. Observations and Models

We created photometric models for the two systems from the WFPC2 and NICMOS V - (F555W), I - (F814W) and H -band (F160W) observations of the two systems by the CfA-Arizona Space Telescope Lens Survey (CASTLES) following the methods of Lehár et al. (2000). The quasars are modeled as point sources and each lens galaxy as a de Vaucouleurs profile. We chose the de Vaucouleurs profile above other models since it provided the best fit. Table 1 summarizes the fits we use here, where the HE1104–1805 model is updated from that in Lehár et al. (2000) using a deeper H -band image obtained to study the quasar host galaxy (Yoo et al. 2006).

For each system we created a sequence of ten lens models using the *lensmodel* software package (Keeton 2001). Each model is the sum of concentric NFW (Navarro, Frenk & White 1996) and de Vaucouleurs components, where the NFW component simulates the dark matter halo and the de Vaucouleurs component represents the galaxy’s stellar content. We parameterize the model sequence by $f_{M/L}$, the mass of the stellar component relative to its mass in a constant mass-to-light ratio model with no contribution from the NFW halo. We generated model sequences covering the range $0.1 \leq f_{M/L} \leq 1.0$. With their time delay measurement, Poindexter et al.

Table 1. HST Astrometry and Photometry of QJ0158–4325 and HE1104–1805

Lens	Component	Astrometry		Photometry		
		Δ RA	Δ Dec	H=F160W	I=F814W	V=F555W
QJ0158–4325	A	$\equiv 0$	$\equiv 0$	16.47 ± 0.03	17.81 ± 0.04	18.10 ± 0.13
	B	$-1''.156 \pm 0''.003$	$-0''.398 \pm 0''.003$	17.27 ± 0.03	18.62 ± 0.11	18.91 ± 0.17
	G	$-0''.780 \pm 0''.016$	$-0''.234 \pm 0''.006$	16.67 ± 0.13	18.91 ± 0.06	20.36 ± 0.18
HE1104–1805	A	$\equiv 0$	$\equiv 0$	15.91 ± 0.01	16.40 ± 0.03	16.92 ± 0.06
	B	$+2''.901 \pm 0''.003$	$-1''.332 \pm 0''.003$	17.35 ± 0.03	17.95 ± 0.04	18.70 ± 0.08
	G	$+0''.965 \pm 0''.003$	$-0''.500 \pm 0''.003$	17.52 ± 0.09	20.01 ± 0.10	23.26 ± 0.27

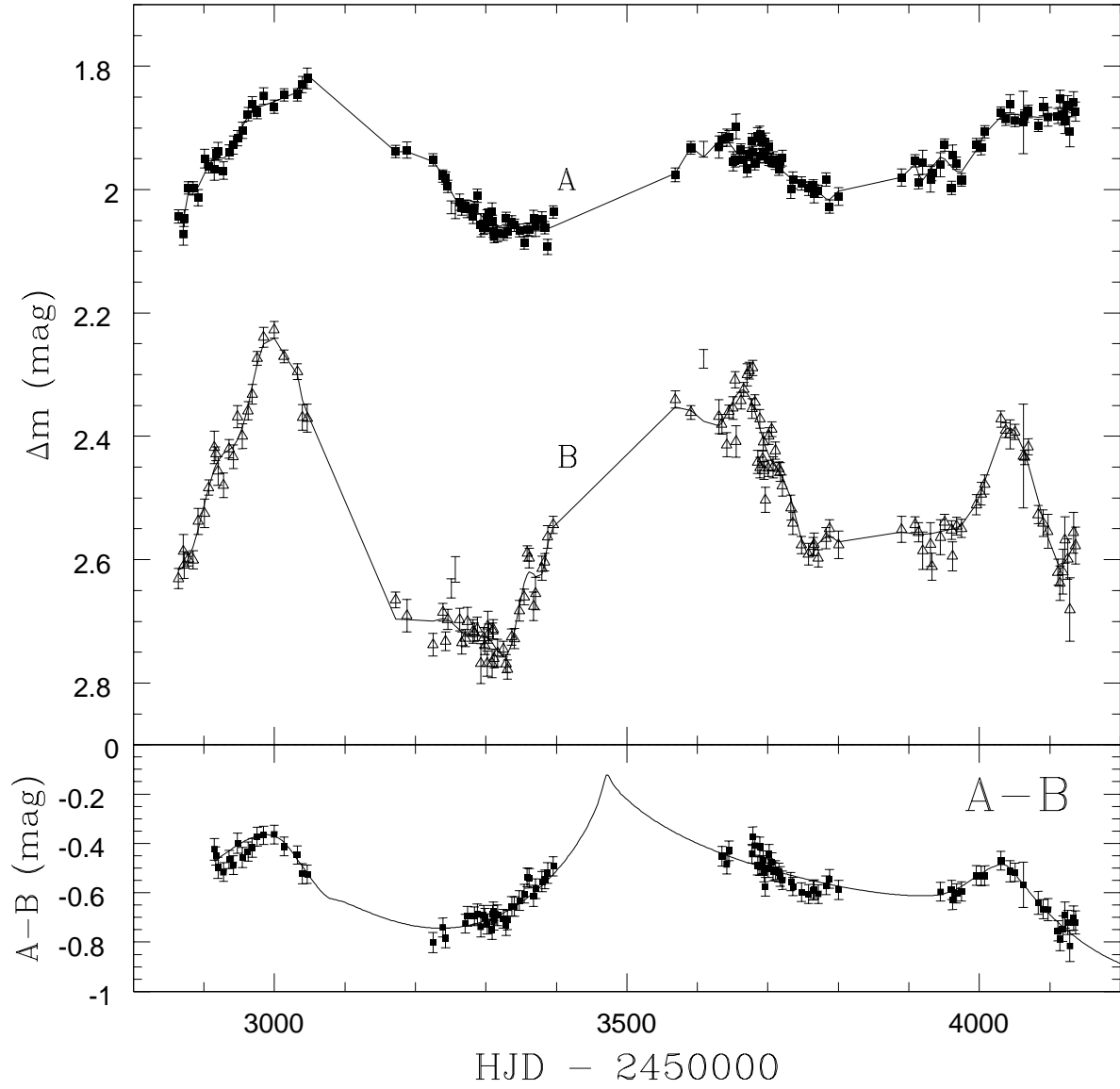


Fig. 1.— Top Panel: QJ0158–4325 *R*-band light curves for images A (squares) and B (triangles). The curves are a polynomial fit to guide the eye. Points with error bars only (no symbols) were not used in the analysis. Lower Panel: Example of a good fit to the implied A–B microlensing signal for a trial time delay of $\Delta t_{AB} = -20$ days.

(2007) constrained the stellar mass fraction of HE1104–1805 to $f_{M/L} = 0.30_{-0.05}^{+0.04}$, but we chose not to apply these limits to $f_{M/L}$ for our present calculations. From these models for the mass distribution we extract the convergence (κ), shear (γ) and stellar surface density (κ_*) for each image and then generate realizations of the microlensing magnification patterns at the location of each image using a variant of the ray-shooting (Schneider et al. 1992) method described in Kochanek (2004). We assume a stellar mass function of $dN(M)/dM \propto M^{-1.3}$ with a dynamic range of 50, which approximates the Galactic stellar mass function of Gould (2000). We present the results either making no assumption about the mean mass $\langle M \rangle$ of the stars or by applying a prior that it lies in the range $0.1 M_\odot \leq \langle M \rangle \leq 1.0 M_\odot$. We used 4096^2 magnification patterns with an outer scale of $20R_E$. We used a prior for the relative motions of the observer, lens galaxy, lens galaxy stars and the source based on the projection of the CMB dipole (Kogut et al. 1993) for the observer, the stellar velocity dispersion of the lens set by its Einstein radius, and rms peculiar velocities for the lens and source of $\sigma_p = 235/(1+z)$ km s $^{-1}$ (Kochanek 2004). We modeled the continuum emission source as a face-on thin accretion disk (Shakura & Sunyaev 1973) with the surface brightness profile

$$I(R) \propto \left\{ \exp \left[(R/r_s)^{3/4} \right] - 1 \right\}^{-1}. \quad (1)$$

The scale radius r_s is the point where the disk temperature matches the rest frame wavelength of our monitoring band, $kT = hc(1+z_s)/\lambda_{obs}$. For comparisons to other disk models, the half-light radius of $R_{1/2} = 2.44r_s$ should be used, since Mortonson et al. (2005) have shown that half-light radii estimated from microlensing depend little on the assumed surface brightness profile of the disk.

We monitored QJ0158–4325 in the R -band using the SMARTS 1.3m telescope with the ANDICAM optical/infrared camera (DePoy et al. 2003)² and using the 1.2m Euler Swiss Telescope as a part of the the COSMOGRAIL³ project. A full description of our monitoring data reduction technique can be found in Kochanek et al. (2006), but we provide a brief summary here. We model the PSF of each quasar image using three nested, elliptical Gaussian components, keeping the relative astrometry fixed for all epochs. We use relative photometry, comparing the flux of each image to the flux of several reference stars in each frame. The lens galaxy flux is determined by optimizing its flux in observations with good seeing, and the light curves are then measured with the galaxy flux fixed to this optimal value. We eliminated all data points taken at seeing conditions worse than $1''.7$. We dropped 3 epochs that satisfied the seeing conditions but on which the sky was very bright. On these nights, the flux measurements from the dimmer image B are clearly contaminated by sky flux, so we report these measurements but chose not to include them in our microlensing analysis. The monitoring data are presented in Table 2, and the light curves are displayed in Figure 1. For HE1104–1805, we use the composite R - and V -band light curve data from Poindexter et al. (2007).

²<http://www.astronomy.ohio-state.edu/ANDICAM/>

³<http://www.cosmograil.org/>

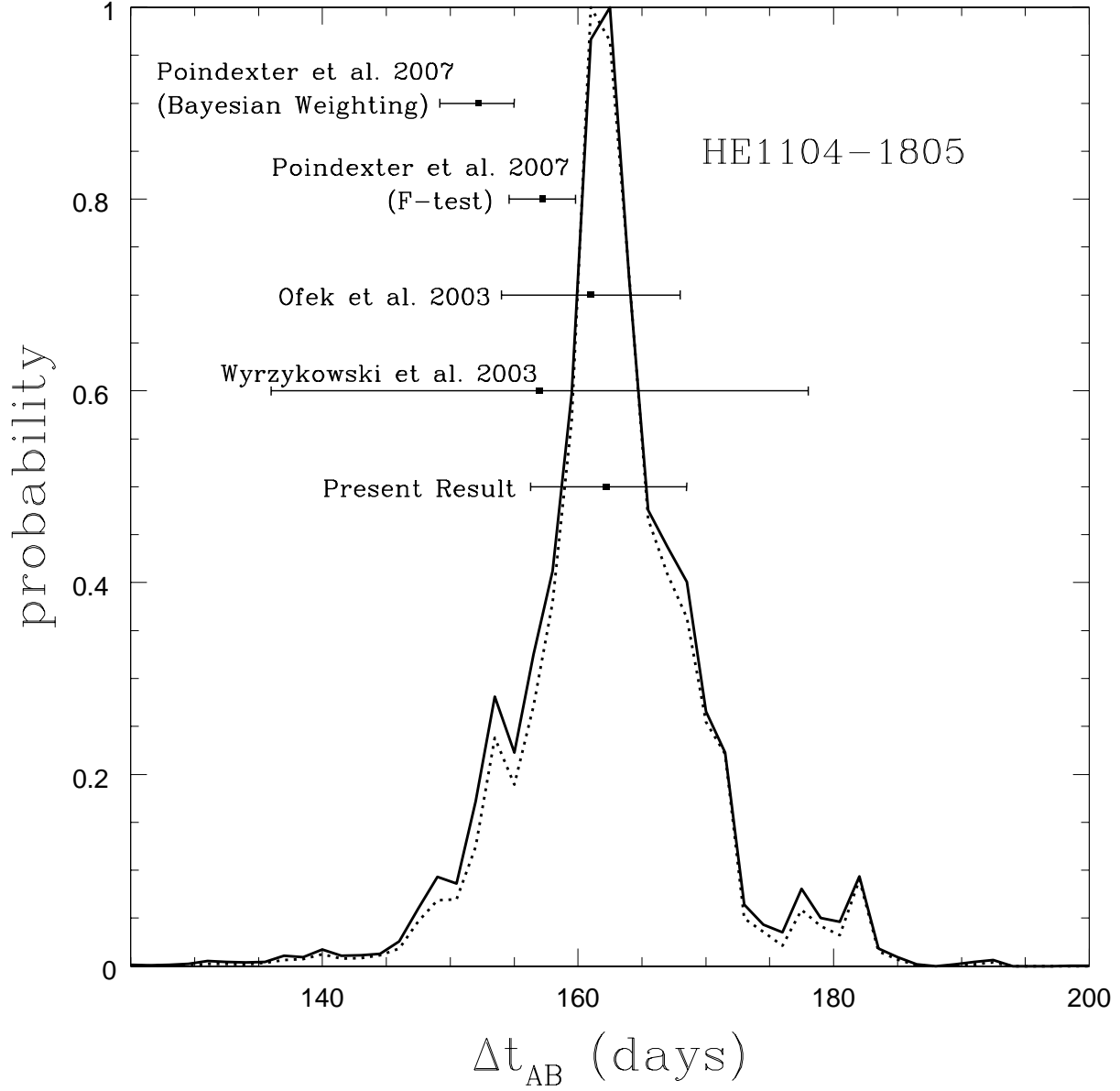


Fig. 2.— Probability distribution for the time delay of HE1104-1805, where $\Delta t_{AB} = t_A - t_B$. The solid curve has no prior on the microlens mass scale while the dotted curve assumes a uniform prior on the mass over the range $0.1 M_\odot \leq \langle M \rangle \leq 1.0 M_\odot$. Previous measurements of the time delay are also plotted. The dependence of the Poindexter et al. (2007) results on the statistical test used demonstrates the limitations of polynomial fitting methods.

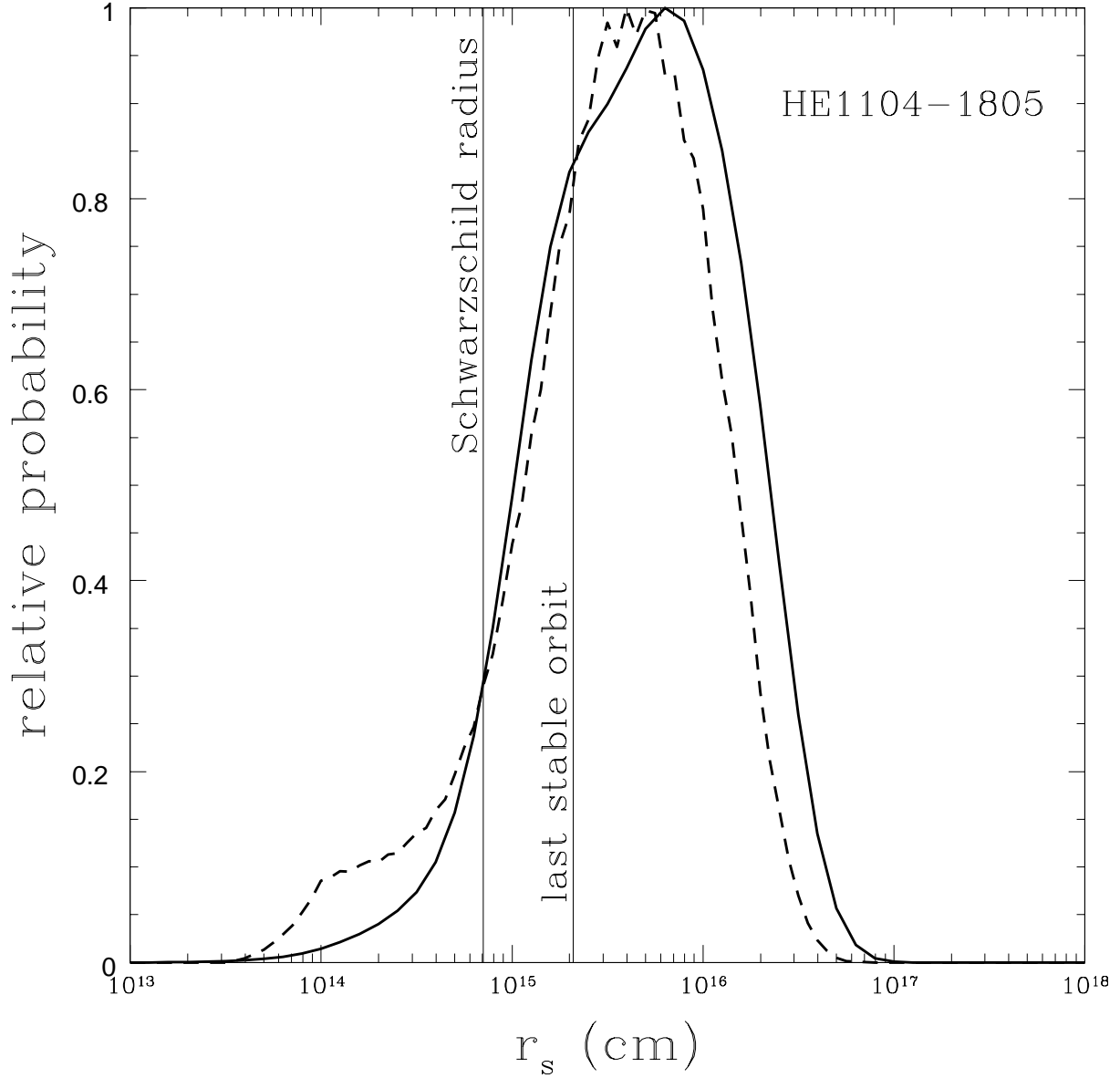


Fig. 3.— Probability distributions for the source size r_s of HE1104–1805. The dashed curve shows the estimate for r_s with a prior of $0.1 M_\odot \leq \langle M \rangle \leq 1.0 M_\odot$ on the mean mass of the microlenses. The vertical line shows the Schwarzschild radius $R_{BH} = 2GM_{BH}/c^2$ of the black hole, where the black hole mass $M_{BH} = 2.37 \times 10^9 M_\odot$ was estimated by Peng et al. (2006) using the C IV emission line width. The last stable orbit for a Schwarzschild black hole is at $3R_{BH}$.

3. Joint Monte Carlo Analysis

For our analysis we must generate light curve pairs with arbitrary delays. We always carry out the shifts on the less variable light curve (image A for both HE1104–1805 and QJ0158–4325). There are two issues for generating the light curves. First, we must define the algorithms for interpolating and extrapolating a light curve, and second we must decide how many extrapolated points should be used. When data points are shifted in the middle of an observing season, we estimate the flux at the shifted time using linear interpolation between the nearest bracketing data points. When shifted points lie in an inter-season gap or beyond either end of the observed lightcurve, we estimate the flux using extrapolation based on a linear fit to the five nearest data points. Data points requiring extrapolation for periods longer than seven days are discarded. We assign new uncertainties that combine the photometric errors with the uncertainties due to the temporal distance of the new point from existing data points, where we model the source variability using the quasar structure function of Vanden Berk et al. (2004).

For a standard analysis, we wanted to use light curves with the same number of data points for each time delay and no points extrapolated by more than seven days. We limit the use of extrapolated points because they lead to a delay-dependent change in the statistical weights caused by the steadily growing uncertainties from the structure function. Given the delay range we wanted to test, we first found the limiting delay defined by the delay which yielded the minimum number of usable data points given our seven day extrapolation limit. We then restricted all of the trial light curves to use only the epochs permissible at the limiting delay. For the very long delays of HE1104–1805, the limiting delay is not the longest delay, because the longest delays shift curves completely through the inter-season gaps. This forced us to restrict the HE1104–1805 analysis to the epochs permitted by both the limiting delay and the longest delay, since some permissible times at the end of the limiting delay lightcurve are beyond the extrapolation limit in light curves with longer delays. We also experimented with simply allowing unlimited extrapolations.

We then analyzed the light curves using the Bayesian Monte Carlo method of Kochanek (2004). In essence, we randomly select a time delay Δt , a lens model and a disk model (size), generate a microlensing light curve and fit it to the microlensing light curve implied by the observed data and the selected time delay. This gives us a χ^2 -statistic for the goodness of fit for the trial $\chi^2(\vec{p}, \Delta t)$ given the model parameters for the microlensing $\vec{p} = (f_{M/L}, r_s, \text{velocities, masses etc.})$ and the time delay. Figure 1 shows an example of a good trial lightcurve fit to QJ 0158–4325 for a delay of $\Delta t_{AB} = -20$ days. In essence, the probability of time delay Δt is the Bayesian integral

$$P(\Delta t|D) \propto \int P(D|\vec{p}, \Delta t)P(\vec{p})P(\Delta t)d\vec{p} \quad (2)$$

where $P(D|\vec{p}, \Delta t)$ is the probability of fitting the data in a particular trial, $P(\vec{p})$ sets the priors on the microlensing variables (see Kochanek 2004; Kochanek et al. 2007) and $P(\Delta t)$ is the (uniform) prior on the time delay. The total probability is then normalized so that $\int P(\Delta t|D)d\Delta t = 1$. We evaluated the integral as a Monte Carlo sum over the trial light curves, where we created

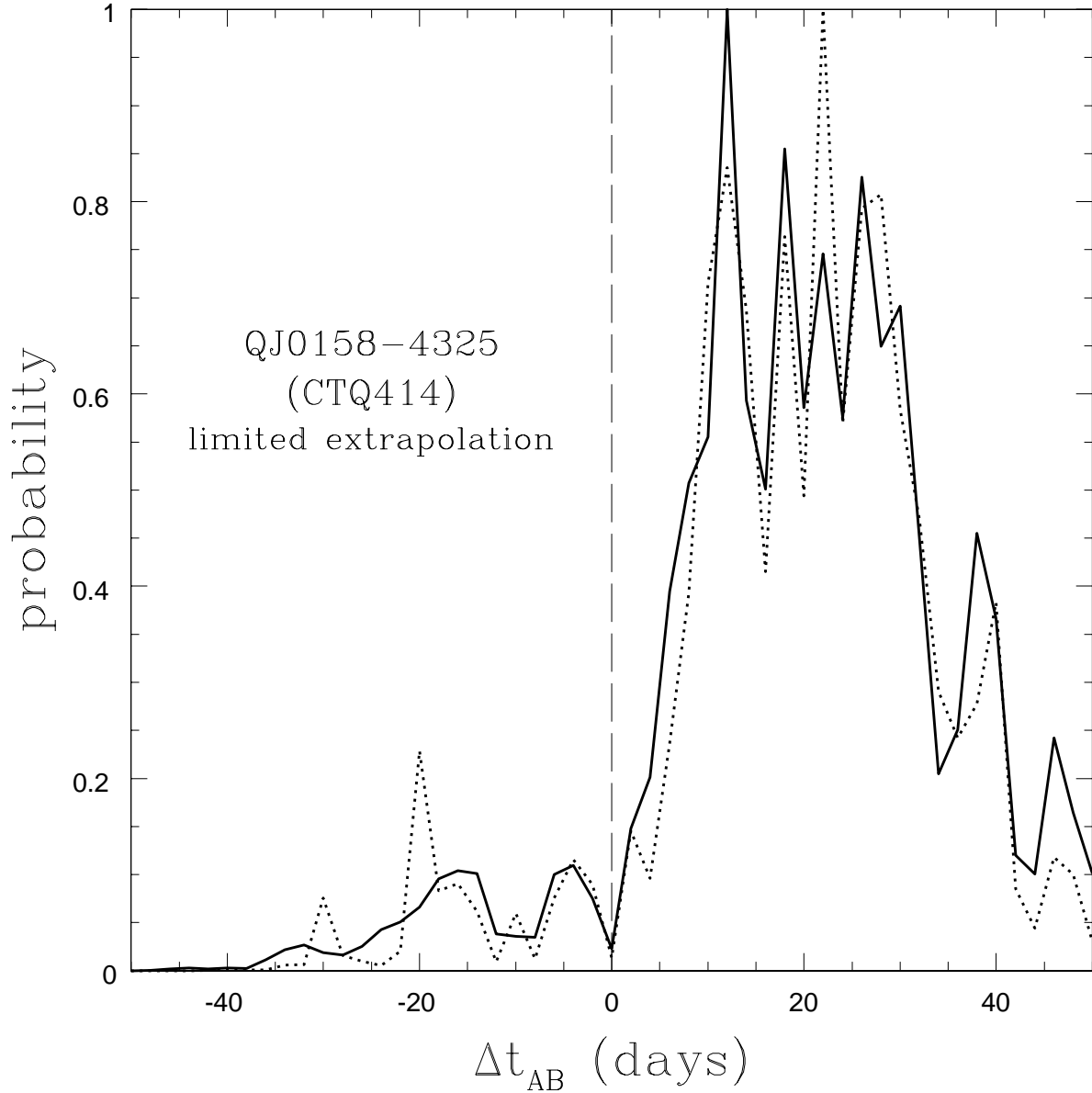


Fig. 4.— Probability distribution for the time delay $\Delta t_{AB} = t_A - t_B$ in QJ0158-4325, where we restrict the extrapolation of the light curves to be less than 7 days. The solid curve assumes no prior on the microlens mass and the dashed curve assumes a uniform prior over the range $0.1 M_\odot \leq \langle M \rangle \leq 1.0 M_\odot$.

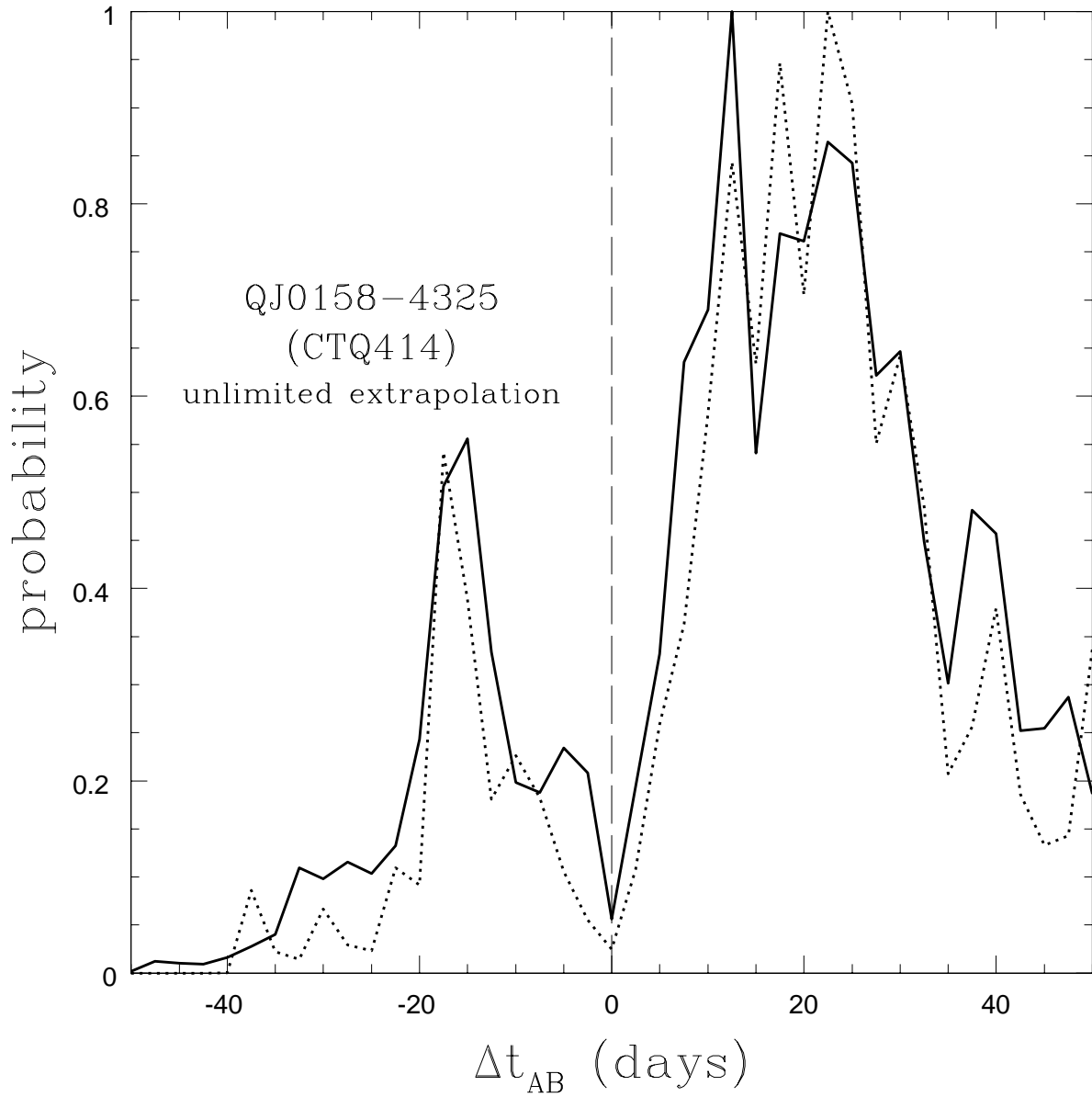


Fig. 5.— Same as Fig. 4, but the trial light curves were generated with no limits on extrapolation. Note the change in the relative probability of positive and negative delays.

4 independent sets of magnification patterns for each of the ten macroscopic mass models and generated 4×10^6 trial light curves for each magnification pattern set.

4. Results

Poindexter et al. (2007) recently estimated a time delay for HE1104–1805 of $\Delta t_{AB} = t_A - t_B = 152.2_{-3.0}^{+2.8}$ days, in the sense that image A lags image B, improving on the earlier estimates by Ofek & Maoz (2003) and Wyrzykowski et al. (2003). The Poindexter et al. (2007) analysis used the Kochanek et al. (2006) polynomial method on light curves which combined the published data of Schechter et al. (2003), Ofek & Maoz (2003) and Wyrzykowski et al. (2003) with new *R*-band monitoring data. In this polynomial method, the source and microlensing variability are modeled as a set of Legendre polynomials that are then fit to the light curves. Ambiguities arise because the value of the delay depends weakly on the parameterization of the microlensing. Poindexter et al. (2007) used a Bayesian weighting scheme for the different polynomial orders, but obtained 157.2 ± 2.6 days if they used the F-test to select among the different orders rather than a Bayesian weighting. The advantage of our present approach is that it uses a physical model for the microlensing rather than a polynomial parameterization of it.

We applied our joint Monte Carlo analysis technique to HE1104–1805 over a time interval range of $125 \text{ days} \leq \Delta t_{AB} \leq 200 \text{ days}$ with a sampling in 1.5 day intervals and no extrapolation of the light curves past 7 days. Figs. 2 and 3 show the resulting probability distributions for the time delay and the disk size. We find a time delay of $\Delta t_{AB} = t_A - t_B = 162.2_{-5.9}^{+6.3}$ days (1σ) that is in marginal agreement with the formal Poindexter et al. (2007) result but in better agreement with the F-test selection of the best polynomial model than with the Bayesian result. Assuming $H_0 = 70 \text{ km s}^{-1} \text{ Mpc}^{-1}$ and an inclination angle of $\cos(i) = 1/2$, the disk size estimate of $\log(r_s/\text{cm}) = 15.7_{-0.5}^{+0.4}$ at $0.2 \mu\text{m}$ in the rest frame is little changed from the estimates in Morgan et al. (2007) and Poindexter, Morgan & Kochanek (2007) which held the delay fixed to the Poindexter et al. (2007) value. The uncertainties in the size are a factor of 1.6 larger in the present analysis.

In models of QJ0158–4325, we expect image A to lead image B by 2–3 weeks depending on the mass distribution and the actual lens redshift (we assumed $z_l = 0.5$). For completeness, we tested a full range of negative and positive delays $-50 \text{ days} \leq \Delta t_{AB} \leq 50 \text{ days}$ at 2 day intervals. We generated the positive and negative delay light curves separately in order to minimize the number of points lost due to the 7 day extrapolation limit at the price of making the data used for positive and negative delays somewhat different. For comparison, we also tried using all points with no extrapolation limits.

Figs. 4 – 6 show the results for the time delays and the source size. We have clearly failed to measure a time delay, and positive delays $\Delta t_{AB} = t_A - t_B$ seem to be favored over negative delays, in direct disagreement with the predictions of the lens model. The relative likelihoods of positive and negative delays depend on the detailed treatment of the light curves, with the probability of positive

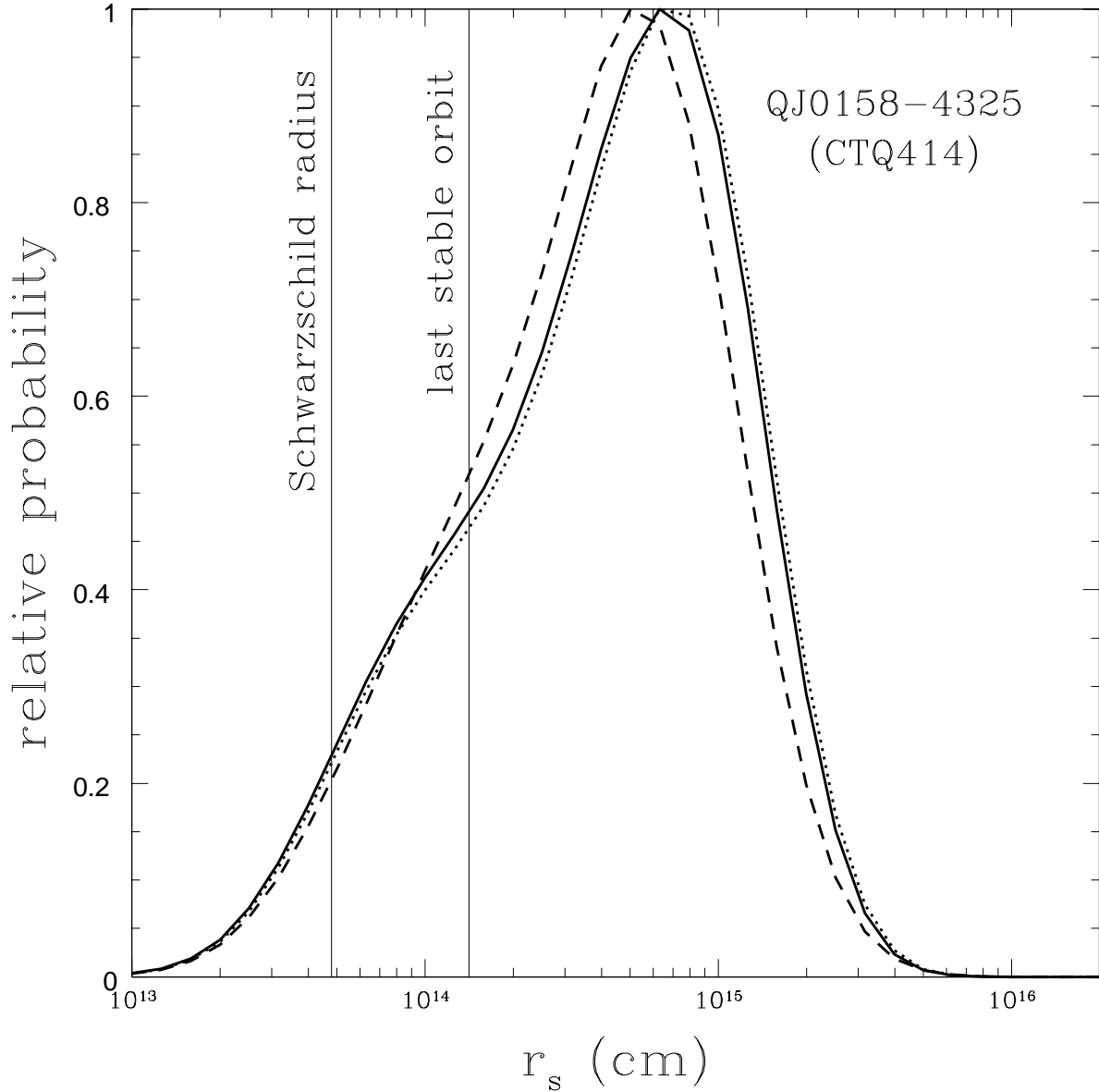


Fig. 6.— Probability distributions for source size r_s of QJ0158-4325. The dashed (dotted) curve shows the estimate for r_s using the set of negative (positive) trial time delays. The solid curve is the r_s estimate using all trial time delays. The vertical line shows the Schwarzschild radius $R_{BH} = 2GM_{BH}/c^2$ of the black hole, where the black hole mass $M_{BH} = 1.6 \times 10^8 M_\odot$ was estimated by Peng et al. (2006) using the Mg II emission line width. The last stable orbit for a Schwarzschild black hole is at $3R_{BH}$.

delays being lower when we use all extrapolated points rather than restricting them to 7 days or less. In this case, the microlensing simply overwhelms the intrinsic variability. We expect additional monitoring data to continue to tighten the time delay probability distribution, but a successful delay measurement may not be possible for many seasons. We succeed, however, in estimating a size for the quasar despite the uncertainties in the time delay, finding a size of $\log(r_s/\text{cm}) = 14.9 \pm 0.3$ at $0.3 \mu\text{m}$ in the rest frame (again, assuming $H_0 = 70 \text{ km s}^{-1} \text{ Mpc}^{-1}$ and $\cos(i) = 1/2$). The size estimate changes little compared to the uncertainties if we limit the analysis to either positive or negative delays. The microlensing amplitudes are large enough that interpreting varying amounts of the lower amplitude intrinsic variability as microlensing does not change the statistics of the microlensing enough to significantly affect the size estimate. One additional uncertainty in this result is that lens redshift of QJ0158–4325 is unknown. We experimented with running the Monte Carlo simulation at a range of lens redshifts ($0.1 \leq z_l \leq 0.9$), and we found that the resulting shifts in the r_s estimates were negligible relative to the size of the existing uncertainties.

5. Discussion and Conclusions

Peng et al. (2006) used the width of the C IV ($\lambda 1549\text{\AA}$) emission line to estimate the black hole mass $M_{BH} = 2.37 \times 10^9 M_\odot$ in HE1104–1805 and the width of Mg II ($\lambda 2798\text{\AA}$) emission line to estimate the black hole mass $M_{BH} = 1.6 \times 10^8 M_\odot$ in QJ0158–4325. Using these black hole masses, the quasar accretion disk size - black hole mass relation of Morgan et al. (2007) predicts source sizes at 2500\AA of $\log(r_s/\text{cm}) = 15.9 \pm 0.2$ for HE1104–1805 and $\log(r_s/\text{cm}) = 15.2 \pm 0.2$ for QJ0158–4325. If we scale our current disk size measurements to 2500\AA using the $R_\lambda \propto \lambda^{4/3}$ scaling of thin disk theory and assume an inclination angle $\cos i = 1/2$, we find $\log(r_s/\text{cm}) = 15.9_{-0.5}^{+0.4}$ for HE1104–1805 and $\log(r_s/\text{cm}) = 14.8 \pm 0.3$ for QJ0158–4325, fully consistent with the predictions of the Morgan et al. (2007) accretion disk size - black hole mass relation.

The mixing of intrinsic and microlensing variability in lensed quasar light curves can be a serious problem for estimating time delays (e.g. Eigenbrod et al. 2005) and previous microlensing analyses have been restricted to lenses with known time delays. In HE1104–1805, which must be close to the limits of measuring time delays in the presence of microlensing, we confirm that the approach of fitting polynomial models for the microlensing works reasonably well. However, the dependence of the delay on the assumed model was a warning sign that the formal errors on the delays were likely to be underestimates, as was recognized by Poindexter et al. (2007). In our new, non-parametric microlensing analysis of HE1104–1805 we find a modestly longer delay of $162.2_{-5.9}^{+6.3}$ days that quantifies those concerns. Estimates of the quasar accretion disk size are little affected by these small shifts in the time delay. In QJ0158–4325, the microlensing amplitude is larger relative to the intrinsic variability, and traditional methods for determining delays fail. Our new method also fails to measure a delay, but it does allow us to measure the size of the quasar accretion disk despite the uncertainties in the time delay.

We thank S. Poindexter for helpful discussions about HE1104–1805 and D. Will for answers to countless cluster computing questions. M.E.E. is grateful for summer internship support from the USNA Bowman Scholar program. C.V., F.C. and G.M. acknowledge support from the Swiss National Science Foundation (SNSF). This research made extensive use of a Beowulf computer cluster obtained through the Cluster Ohio program of the Ohio Supercomputer Center. Support for program HST-GO-9744 was provided by NASA through a grant from the Space Telescope Science Institute, which is operated by the Association of Universities for Research in Astronomy, Inc., under NASA contract NAS-5-26666.

Facilities: CTIO:2MASS (ANDICAM), HST (NICMOS, ACS), Swiss 1.2m Telescope

REFERENCES

- Burud, I., Magain, P., Sohy, S. & Hjorth, J. 2001, *A&A*, 380, 805
- Dai, X. Kochanek, C.S., Chartas, G., Morgan, N.D. Morgan, C.W. & Garmire, G.P.. 2007, in preparation
- DePoy, D.L., Atwood, B., Belville, S.R., Brewer, D.F., Byard, P.L., Gould, A., Mason, J.A., O’Brien, T.P., Pappalardo, D.P., Pogge, R.W., Steinbrecher, D.P., & Tiega, E.J. 2003, *Proc. SPIE*, 4841, 827
- Eigenbrod, A., Courbin, F., Vuissoz, C., Meylan, G., Saha, P. & Dye, S. 2005, *A&A*, 436, 25
- Freedman, W. et al., 2001, *ApJ*, 553, 47
- Keeton, C.R. 2001, preprint (astro-ph/0102340)
- Kochanek, C.S. 2004, *ApJ*, 605, 58
- Kochanek, C.S., Morgan, N.D., Falco, E.E. McLeod, B.A., Winn, J. Dembicky, J. & Ketzbeck, B. 2006, *ApJ*, 640, 47
- Kochanek, C.S., Dai, X., Morgan, C.W., Morgan, N.D., Poindexter, S.A., Chartas, G. 2007, in *Statistical Challenges in Astronomy IV*, ed. G.J. Babu & E.D. Feigelson, (San Francisco:ASP), in press
- Kogut, A., et al. 1993, *ApJ*, 419, 1
- Fohlmeister, J. et al. 2007, *ApJ*, 662, 62
- Gould, A. 2000, *ApJ*, 535, 928
- Lehár, J., Falco, E.E, Kochanek, C.S., McLeod, B.A., Impey, C.D., Rix, H.-W., Keeton, C.R. & Peng, C.Y. 2000, *ApJ*, 536, 584

- Morgan, C.W., Kochanek, C.S., Morgan, N.D. & Falco, E.E. ApJ, submitted
- Morgan, N.D., Dressler, A., Maza, J., Schechter, P.L. & Winn, J.N. 1999, AJ, 118, 1444
- Mortonson, M.J., Schechter, P.L. & Wambsganss, J. 2005, ApJ, 628, 594
- Navarro, J.F. Frenk, C.S. & White S.D.M. 1996, ApJ, 462, 563
- Ofek, E.O. & Maoz, D. 2003, ApJ, 594, 101
- Oguri, M. 2007, ApJ, 660, 1
- Paraficz D., Hjorth J., Burud I., Jakobsson P., Elíasdóttir Á. 2006, A&A, 455, L1
- Peng, C.Y., Impey, C.D., Rix, H.-W., Kochanek, C.S., Keeton, C.S., Falco, E.E., Lehár, J. & McLeod, B.A. 2006, ApJ, 649, 616
- Poindexter, S. Morgan, N.D., Kochanek, C.S. & Falco, E.E 2007, ApJ, 660, 146
- Poindexter, S. Morgan, N.D. & Kochanek, C.S. 2007, ApJ, in press
- Pooley,, D, Blackburne, J.A., Rappaport, S., Schechter, P.L. & Fong, W.-F. 2006, ApJ, 648, 67
- Pooley, D., Blackburne, J. A., Rappaport, S. & Schechter, P.L. 2007 ApJ, 661, 19
- Refsdal, S. 1964, MNRAS, 128,307
- Saha, P, Coles, J., Macció, A.V. & Williams, L.L.R. 2006, ApJ, 650, L17
- Schechter, P.L. et al. 1997, ApJ, 475, L85
- Schechter P. L., Wambsganss J. 2002, ApJ, 580, 685
- Schechter, P.L., et al. 2003, ApJ, 584, 657
- Schneider, P., Ehlers, J. & Falco, E.E. 1992, Gravitational Lenses (Berlin:Springer)
- Shakura, N.I. & Sunyaev, R.A. 1973, A&A, 24, 337
- Vanden Berk, D.E. et al. 2004, ApJ, 601, 692
- Vuissoz, C. et al. 2007, A&A, 464, 845
- Wambsganss, J. 2006, in Saas-Fee Advanced Course 33, Gravitational Lensing: Strong, Weak and Micro, ed. G. Meylan, P. Jetzer. & P. North, (Berlin:Springer)
- Wisotzki, L., Koehler, T., Kayser, R & Reimers, D. 1993, A&A, 278, L15
- Wyrzykowski, L. et al. 2003, Acta Astron., 53, 229

Yoo, J. Kochanek., C.S., Falco, E.E. & McLeod, B.A. 2006, ApJ, 642, 22

Table 2. QJ0158–4325 Light curves

HJD	χ^2/N_{dof}	QSO A (mags)	QSO B (mags)	$\langle \text{Stars} \rangle$	Source
2863.873	1.17	2.043 ± 0.010	2.631 ± 0.015	-0.059 ± 0.003	SMARTS
2870.788	1.93	2.072 ± 0.013	2.585 ± 0.020	-0.063 ± 0.003	SMARTS
2871.813	0.66	2.046 ± 0.014	2.609 ± 0.022	-0.063 ± 0.004	SMARTS
2877.772	1.01	1.997 ± 0.008	2.600 ± 0.011	0.017 ± 0.003	SMARTS
2884.771	2.15	1.998 ± 0.007	2.600 ± 0.010	0.023 ± 0.003	SMARTS
2891.770	0.83	2.014 ± 0.013	2.537 ± 0.021	-0.068 ± 0.003	SMARTS
2900.798	2.26	1.950 ± 0.010	2.524 ± 0.015	-0.041 ± 0.003	SMARTS
2906.761	1.75	1.962 ± 0.007	2.483 ± 0.009	0.025 ± 0.003	SMARTS
2914.653	0.49	1.968 ± 0.018	2.417 ± 0.026	-0.045 ± 0.004	SMARTS
2916.766	1.00	1.942 ± 0.008	2.429 ± 0.011	-0.006 ± 0.003	SMARTS
2919.787	0.55	1.938 ± 0.014	2.455 ± 0.023	-0.072 ± 0.003	SMARTS
2927.729	2.38	1.969 ± 0.009	2.479 ± 0.013	-0.022 ± 0.003	SMARTS
2935.680	2.25	1.939 ± 0.008	2.420 ± 0.010	0.010 ± 0.003	SMARTS
2941.674	3.82	1.928 ± 0.008	2.433 ± 0.010	0.018 ± 0.003	SMARTS
2947.635	0.73	1.916 ± 0.012	2.368 ± 0.018	-0.054 ± 0.003	SMARTS
2954.626	0.85	1.903 ± 0.013	2.400 ± 0.020	-0.064 ± 0.004	SMARTS
2962.598	1.28	1.878 ± 0.010	2.359 ± 0.013	-0.038 ± 0.003	SMARTS
2968.621	3.01	1.862 ± 0.007	2.332 ± 0.009	-0.008 ± 0.003	SMARTS
2975.577	2.02	1.875 ± 0.007	2.273 ± 0.008	0.012 ± 0.003	SMARTS
2984.541	3.28	1.848 ± 0.007	2.239 ± 0.009	0.016 ± 0.003	SMARTS
2999.619	1.54	1.866 ± 0.009	2.227 ± 0.011	0.010 ± 0.003	SMARTS
3013.587	0.92	1.846 ± 0.008	2.271 ± 0.011	-0.030 ± 0.003	SMARTS
3032.567	1.70	1.846 ± 0.008	2.295 ± 0.010	0.011 ± 0.003	SMARTS
3039.534	1.34	1.830 ± 0.011	2.369 ± 0.018	-0.068 ± 0.003	SMARTS
3046.543	4.29	1.820 ± 0.008	2.371 ± 0.011	0.006 ± 0.003	SMARTS
3171.930	0.92	1.938 ± 0.008	2.666 ± 0.013	-0.010 ± 0.003	SMARTS
3187.869	0.65	1.934 ± 0.013	2.694 ± 0.026	-0.068 ± 0.003	SMARTS
3224.869	0.70	1.950 ± 0.010	2.743 ± 0.018	-0.024 ± 0.003	SMARTS
3238.825	0.99	1.977 ± 0.009	2.688 ± 0.014	0.004 ± 0.003	SMARTS
3242.777	0.76	1.981 ± 0.009	2.732 ± 0.015	-0.026 ± 0.003	SMARTS
3245.784	0.61	1.994 ± 0.010	2.698 ± 0.016	-0.051 ± 0.003	SMARTS
3250.779	1.29	(2.029 ± 0.009)	(2.646 ± 0.014)	-0.042 ± 0.003	SMARTS
3256.852	0.80	(2.035 ± 0.013)	(2.616 ± 0.021)	-0.044 ± 0.003	SMARTS

Table 2—Continued

HJD	χ^2/N_{dof}	QSO A (mags)	QSO B (mags)	$\langle \text{Stars} \rangle$	Source
3262.779	3.42	2.020 ± 0.007	2.697 ± 0.010	0.020 ± 0.003	SMARTS
3265.790	1.82	2.030 ± 0.008	2.735 ± 0.013	-0.002 ± 0.003	SMARTS
3270.792	1.46	2.027 ± 0.008	2.727 ± 0.011	0.013 ± 0.003	SMARTS
3273.731	1.68	2.031 ± 0.011	2.701 ± 0.018	-0.048 ± 0.003	SMARTS
3281.769	1.52	2.043 ± 0.010	2.716 ± 0.016	-0.037 ± 0.003	SMARTS
3283.759	1.65	2.029 ± 0.008	2.718 ± 0.011	0.001 ± 0.003	SMARTS
3287.633	0.73	2.009 ± 0.011	2.715 ± 0.019	-0.015 ± 0.003	SMARTS
3292.735	2.96	2.057 ± 0.011	2.769 ± 0.019	-0.038 ± 0.003	SMARTS
3296.721	2.25	2.061 ± 0.008	2.726 ± 0.011	0.009 ± 0.003	SMARTS
3298.691	1.36	2.060 ± 0.008	2.740 ± 0.012	-0.001 ± 0.003	SMARTS
3301.686	0.84	2.044 ± 0.011	2.769 ± 0.020	-0.058 ± 0.003	SMARTS
3302.791	0.98	2.052 ± 0.013	2.707 ± 0.024	-0.016 ± 0.003	EULER
3303.690	0.80	2.041 ± 0.010	2.720 ± 0.016	-0.052 ± 0.003	SMARTS
3308.686	2.29	2.035 ± 0.009	2.768 ± 0.015	-0.016 ± 0.003	EULER
3309.642	0.58	2.051 ± 0.009	2.717 ± 0.013	-0.026 ± 0.003	SMARTS
3310.580	1.51	2.067 ± 0.008	2.713 ± 0.012	0.025 ± 0.003	EULER
3311.639	1.88	2.076 ± 0.008	2.760 ± 0.011	0.014 ± 0.003	SMARTS
3316.694	0.59	2.071 ± 0.013	2.752 ± 0.022	-0.050 ± 0.003	SMARTS
3324.630	1.37	2.072 ± 0.008	2.745 ± 0.011	0.005 ± 0.003	SMARTS
3328.616	0.66	2.046 ± 0.009	2.769 ± 0.015	-0.018 ± 0.003	SMARTS
3330.629	1.05	2.068 ± 0.009	2.779 ± 0.015	-0.034 ± 0.003	SMARTS
3336.600	0.88	2.052 ± 0.009	2.726 ± 0.013	-0.035 ± 0.003	SMARTS
3340.603	0.96	2.058 ± 0.010	2.728 ± 0.016	-0.008 ± 0.003	SMARTS
3347.574	0.83	2.065 ± 0.010	2.685 ± 0.017	-0.010 ± 0.003	SMARTS
3354.564	1.45	2.086 ± 0.008	2.661 ± 0.011	0.007 ± 0.003	SMARTS
3358.560	1.00	2.064 ± 0.009	2.592 ± 0.012	-0.012 ± 0.003	SMARTS
3361.553	0.73	2.063 ± 0.011	2.600 ± 0.016	-0.043 ± 0.003	SMARTS
3367.572	0.62	2.046 ± 0.014	2.677 ± 0.023	-0.066 ± 0.004	SMARTS
3370.582	2.26	2.057 ± 0.011	2.658 ± 0.018	-0.030 ± 0.003	SMARTS
3379.581	0.55	2.046 ± 0.012	2.619 ± 0.020	-0.017 ± 0.003	SMARTS
3383.581	1.32	2.062 ± 0.009	2.604 ± 0.012	-0.002 ± 0.003	SMARTS
3387.563	0.63	2.092 ± 0.012	2.566 ± 0.018	-0.043 ± 0.003	SMARTS
3395.547	0.86	2.036 ± 0.010	2.544 ± 0.014	-0.062 ± 0.003	SMARTS

Table 2—Continued

HJD	χ^2/N_{dof}	QSO A (mags)	QSO B (mags)	$\langle \text{Stars} \rangle$	Source
3568.889	1.66	1.976 ± 0.009	2.340 ± 0.011	-0.018 ± 0.003	SMARTS
3590.890	1.19	1.932 ± 0.008	2.362 ± 0.010	-0.003 ± 0.003	SMARTS
3608.820	4.55	(1.935 ± 0.006)	(2.274 ± 0.007)	0.112 ± 0.002	EULER
3630.626	0.75	1.929 ± 0.018	2.370 ± 0.027	-0.053 ± 0.004	SMARTS
3634.802	0.86	1.918 ± 0.011	2.382 ± 0.016	-0.063 ± 0.003	SMARTS
3641.753	2.01	1.916 ± 0.010	2.414 ± 0.014	-0.016 ± 0.003	SMARTS
3644.792	0.91	1.914 ± 0.008	2.360 ± 0.010	-0.007 ± 0.003	SMARTS
3653.595	1.43	1.953 ± 0.009	2.309 ± 0.011	-0.028 ± 0.003	SMARTS
3661.717	0.77	1.936 ± 0.010	2.342 ± 0.013	-0.067 ± 0.003	SMARTS
3665.707	0.91	1.952 ± 0.009	2.324 ± 0.011	-0.041 ± 0.003	SMARTS
3670.620	1.53	1.964 ± 0.011	2.302 ± 0.015	-0.022 ± 0.003	SMARTS
3673.595	0.81	1.942 ± 0.011	2.294 ± 0.013	-0.037 ± 0.003	SMARTS
3677.661	3.41	1.922 ± 0.007	2.355 ± 0.009	0.131 ± 0.002	EULER
3678.644	1.28	1.939 ± 0.009	2.290 ± 0.011	-0.004 ± 0.003	SMARTS
3681.643	0.88	1.958 ± 0.009	2.345 ± 0.012	-0.033 ± 0.003	SMARTS
3685.669	5.14	1.914 ± 0.006	2.442 ± 0.008	0.079 ± 0.003	EULER
3688.633	0.50	1.944 ± 0.011	2.373 ± 0.015	-0.064 ± 0.003	SMARTS
3688.676	4.26	1.910 ± 0.006	2.451 ± 0.008	0.069 ± 0.003	EULER
3692.631	2.72	1.923 ± 0.006	2.436 ± 0.008	0.094 ± 0.003	EULER
3693.560	2.10	1.941 ± 0.008	2.409 ± 0.010	-0.012 ± 0.003	SMARTS
3694.631	2.43	1.946 ± 0.007	2.455 ± 0.009	0.113 ± 0.002	EULER
3696.623	5.99	1.923 ± 0.006	2.503 ± 0.008	0.135 ± 0.002	EULER
3700.648	2.38	1.931 ± 0.006	2.452 ± 0.009	0.122 ± 0.002	EULER
3701.605	1.01	1.951 ± 0.010	2.400 ± 0.013	-0.021 ± 0.003	SMARTS
3705.652	1.12	1.952 ± 0.009	2.389 ± 0.011	-0.004 ± 0.003	SMARTS
3707.706	2.82	1.951 ± 0.007	2.450 ± 0.010	0.122 ± 0.002	EULER
3710.605	0.99	1.957 ± 0.010	2.424 ± 0.014	-0.012 ± 0.003	SMARTS
3715.693	2.21	1.967 ± 0.006	2.452 ± 0.007	0.105 ± 0.002	EULER
3717.573	0.68	1.953 ± 0.010	2.459 ± 0.015	-0.061 ± 0.003	SMARTS
3720.644	3.80	1.949 ± 0.007	2.480 ± 0.009	0.062 ± 0.003	EULER
3732.631	4.36	1.999 ± 0.007	2.516 ± 0.010	0.121 ± 0.002	EULER
3735.616	4.39	1.985 ± 0.006	2.541 ± 0.009	0.126 ± 0.002	EULER
3747.614	3.03	1.990 ± 0.006	2.576 ± 0.008	0.079 ± 0.003	EULER

Table 2—Continued

HJD	χ^2/N_{dof}	QSO A (mags)	QSO B (mags)	$\langle \text{Stars} \rangle$	Source
3757.606	1.92	1.998 ± 0.008	2.591 ± 0.013	0.088 ± 0.003	EULER
3764.534	0.80	1.994 ± 0.010	2.579 ± 0.015	-0.033 ± 0.003	SMARTS
3765.570	6.22	2.007 ± 0.006	2.575 ± 0.007	0.130 ± 0.002	EULER
3771.604	2.31	2.003 ± 0.006	2.598 ± 0.009	0.091 ± 0.003	EULER
3782.557	1.59	1.984 ± 0.008	2.565 ± 0.013	0.032 ± 0.003	EULER
3787.531	2.82	2.027 ± 0.006	2.549 ± 0.009	0.098 ± 0.003	EULER
3800.519	2.23	2.011 ± 0.010	2.576 ± 0.015	0.032 ± 0.003	EULER
3889.922	2.68	1.980 ± 0.008	2.551 ± 0.013	0.097 ± 0.003	EULER
3908.910	2.44	1.953 ± 0.006	2.543 ± 0.008	0.128 ± 0.002	EULER
3913.839	2.94	1.987 ± 0.007	2.555 ± 0.009	0.102 ± 0.003	EULER
3919.880	5.01	1.956 ± 0.009	2.585 ± 0.014	0.029 ± 0.003	EULER
3930.856	0.49	1.983 ± 0.021	2.577 ± 0.036	-0.016 ± 0.004	SMARTS
3932.920	1.40	1.973 ± 0.011	2.611 ± 0.019	0.007 ± 0.003	EULER
3950.832	2.46	1.928 ± 0.006	2.539 ± 0.008	0.140 ± 0.002	EULER
3960.817	1.23	1.997 ± 0.010	2.552 ± 0.014	-0.051 ± 0.003	SMARTS
3961.922	6.26	1.944 ± 0.006	2.594 ± 0.009	0.093 ± 0.003	EULER
3967.838	0.85	1.957 ± 0.010	2.546 ± 0.014	-0.026 ± 0.003	SMARTS
3974.783	1.11	1.984 ± 0.010	2.550 ± 0.014	-0.030 ± 0.003	SMARTS
3995.765	0.88	1.927 ± 0.011	2.511 ± 0.016	-0.034 ± 0.003	SMARTS
4002.702	1.03	1.931 ± 0.012	2.494 ± 0.018	-0.043 ± 0.003	SMARTS
4007.696	0.70	1.905 ± 0.010	2.479 ± 0.015	-0.032 ± 0.003	SMARTS
4030.632	0.82	1.876 ± 0.010	2.372 ± 0.013	-0.020 ± 0.003	SMARTS
4037.600	0.92	1.886 ± 0.009	2.390 ± 0.012	-0.025 ± 0.003	SMARTS
4043.600	0.48	1.861 ± 0.015	2.397 ± 0.023	-0.063 ± 0.004	SMARTS
4050.620	1.34	1.888 ± 0.008	2.393 ± 0.011	-0.022 ± 0.003	SMARTS
4062.536	0.47	1.891 ± 0.051	2.432 ± 0.084	0.109 ± 0.005	SMARTS
4064.646	0.84	1.881 ± 0.009	2.434 ± 0.012	-0.011 ± 0.003	SMARTS
4069.580	0.82	1.872 ± 0.009	2.419 ± 0.013	-0.049 ± 0.003	SMARTS
4083.542	0.69	1.895 ± 0.010	2.527 ± 0.015	-0.037 ± 0.003	SMARTS
4090.621	2.29	1.865 ± 0.010	2.541 ± 0.014	-0.037 ± 0.003	SMARTS
4097.556	0.40	1.882 ± 0.015	2.554 ± 0.027	-0.059 ± 0.004	SMARTS
4111.601	1.23	1.880 ± 0.011	2.622 ± 0.019	-0.033 ± 0.003	SMARTS
4114.561	1.08	1.842 ± 0.013	2.664 ± 0.027	-0.037 ± 0.003	SMARTS

Table 2—Continued

HJD	χ^2/N_{dof}	QSO A (mags)	QSO B (mags)	$\langle\text{Stars}\rangle$	Source
4118.593	0.48	1.873 ± 0.018	2.628 ± 0.036	-0.055 ± 0.004	SMARTS
4121.529	0.57	1.888 ± 0.020	2.571 ± 0.038	-0.049 ± 0.004	SMARTS
4125.526	0.66	1.863 ± 0.017	2.602 ± 0.033	-0.047 ± 0.004	SMARTS
4128.574	0.51	1.900 ± 0.024	2.696 ± 0.052	-0.047 ± 0.004	SMARTS
4133.581	0.45	1.858 ± 0.017	2.557 ± 0.033	-0.051 ± 0.004	SMARTS
4136.572	0.49	1.873 ± 0.015	2.578 ± 0.030	-0.068 ± 0.004	SMARTS
4301.869	1.05	1.815 ± 0.008	2.565 ± 0.012	0.006 ± 0.003	SMARTS
4307.824	0.70	1.794 ± 0.009	2.571 ± 0.016	-0.041 ± 0.003	SMARTS

Note. — HJD is the Heliocentric Julian Day – 2450000 days. The goodness of fit of the image, χ^2/N_{dof} , is used to rescale the formal uncertainties when greater than unity. The QSO A&B columns give the magnitudes of the quasar images relative to the comparison stars. The $\langle\text{Stars}\rangle$ column gives the mean magnitude of the standard stars for that epoch relative to their mean for all epochs. A few points in the lightcurves (in parentheses) were not used in the analysis.